Journal of Power Sources 196 (2011) 8866–8873

Contents lists available at ScienceDirect

Journal of Power Sources

journal homepage: www.elsevier.com/locate/jpowsour

Self-discharge analysis and characterization of supercapacitors for environmentally powered wireless sensor network applications

Hengzhao Yang, Ying Zhang*

School of Electrical and Computer Engineering, Georgia Institute of Technology, Atlanta, GA 30332, USA

ARTICLE INFO

Article history:
Received 29 April 2011
Received in revised form 11 June 2011
Accepted 11 June 2011
Available online 17 June 2011

Keywords:
Supercapacitor modeling
Self-discharge
Wireless sensor networks

ABSTRACT

A new approach is presented to characterize the variable leakage resistance, a parameter in the variable leakage resistance model we developed to model supercapacitors used in environmentally powered wireless sensor network applications. Based on an analysis of the supercapacitor terminal behavior during the self-discharge, the variable leakage resistance is modeled as a function of the supercapacitor terminal voltage instead of the self-discharge time, which is more practical for an environmentally powered wireless sensor node. The new characterization approach is implemented and validated using MATLAB Simulink with a 10 F supercapacitor as an example. In addition, effects of initial voltages and temperatures on the supercapacitor self-discharge rate and the variable leakage resistance value are explored.

1. Introduction

Wireless sensor networks have been evolving into a key technology for applications such as military surveillance [1] and habitat monitoring [2]. The sensor nodes used in these applications often have low power consumption, low cost and small size. To ensure sustainability, various environmental energy harvesting technologies, such as solar energy [3], mechanical vibration [4], radio frequency energy [5], and wind energy [6], have been proposed to power wireless sensor nodes. These energy harvesting technologies require storage devices to buffer the harvested energy.

Various rechargeable batteries such as NiMH [7] and Li-ion [8] have been used as energy buffers. While rechargeable batteries have high capacity and low leakage rate, the cycle life of rechargeable batteries limit the lifetime of wireless sensor nodes [9]. The cycle life of a rechargeable battery is defined as the number of charge–discharge cycles before its capacity falls below 80% of its initial rated capacity. The aging process during the charge–discharge cycles results in a gradual reduction in capacity and an increase in internal resistance over time [10]. By the end of the cycle life, the capacity of a rechargeable battery is reduced by 20% and the useful energy drops to 50% because the higher internal resistance causes premature end of life [9]. Because of the limited cycle life, typically ranging from 100 to 1000 cycles [11], a wireless sensor node will require battery replacement after one to two years [9].

On the other hand, supercapacitors have certain advantages over rechargeable batteries: a much longer cycle life (can be more than 1,000,000 cycles), higher charge–discharge efficiency, and fast charge–discharge characteristic [12]. The problem with supercapacitors is their relatively high leakage rate [12]. Several systems have been proposed to either use supercapacitors alone [9,12,13] to store the harvested energy or use supercapacitors in combination with rechargeable batteries to leverage the complementary strengths of these two energy buffers [14,15]. Due to wide range of potential applications of environmentally powered wireless sensor networks, considerable research efforts have been made to develop efficient power storage systems [9], power management algorithms [16] and communication protocols [17]. A supercapacitor model is an important tool to evaluate these researches using analytical methods or simulations before they are demonstrated in practical deployments.

Supercapacitors can be modeled using the electrochemical impedance spectroscopy (EIS) technique, which is a general approach to characterize energy storage devices by measuring their complex impedances [18]. The nature of impedances in various frequency ranges can be determined by analyzing the frequency dependencies of the real part and the imaginary part [19]. Various equivalent circuit models [20,21] have been developed that use the porous electrode theory [22–26] to interpret the impedance spectrum of a supercapacitor. With the assumption of homogeneous electrode pore size, a general porous impedance model consists of three impedances linking to electrode, electrolyte and electrode/electrolyte interface, respectively [24,25]. The general model can be modified if interface roughness [27] or random pore size [28] is considered. The impedance spectrum can be modeled by N inter-

* Corresponding author. Tel.: +1 912 963 2572; fax: +1 912 966 7928.
E-mail address: yzhang@gatech.edu (Y. Zhang).

0378-7753/$ – see front matter © 2011 Elsevier B.V. All rights reserved.
doi:10.1016/j.jpowsour.2011.06.042

leaved resistance–capacitance (RC) circuits which would require a calculation of 2*N* parameters [18]. However, it is usually very difficult to determine more than five or six independent parameters efficiently considering their strong influences on each other [18].

Alternatively, supercapacitors can be characterized in time domain by conducting various experiments such as constant power tests and constant current tests [19]. In power electronics applications, this approach is often used to develop an equivalent circuit to model the terminal behavior of a supercapacitor [29,30]. As a supercapacitor is usually constructed with two porous carbon electrodes impregnated with electrolyte and separated by a porous insulating membrane, the interface electrochemistry suggests that a complex network of non-linear capacitances connected by resistances can describe the terminal behavior of a supercapacitor [29]. In this network, resistances represent the resistances of carbon particles and capacitances describe the capacitances between electrodes and electrolyte [30]. In practical applications, simplified versions are required to enable model implementation [29–32].

For wireless sensor network applications, most adopted supercapacitor models are developed based on the supercapacitor leakage power profiles [12,14,33]. These models assume the capacitance of a supercapacitor is constant, and use a leakage power profile to determine the remaining energy stored in the supercapacitor [12]. However, the supercapacitor physics suggests that its capacitance depends on its terminal voltage and the supercapacitor usually experiences internal charge redistribution [30].

In our previous work on supercapacitor modeling and characterization [34], an equivalent circuit model called the variable leakage resistance (VLR) model was developed to describe the supercapacitor terminal behavior, which uses two RC branches with different time constants to characterize the charging-redistribution process, and a variable leakage resistance to characterize the self-discharge process. The variable leakage resistance is determined by fitting the supercapacitor self-discharge with multiple exponential functions. The VLR model was demonstrated to be a more accurate model for environmentally powered wireless sensor network applications.

In our original variable leakage resistance model, the leakage resistance was characterized as a function of the self-discharge time. In practice, it is preferred to have model parameters that depend on the supercapacitor terminal voltage, which can be measured on a real time basis, instead of the self-discharge time, which requires recording and tracking the past states of the supercapacitor. In this paper, a new parameter determination process for the variable leakage resistance is proposed. Additionally, the effects of supercapacitor initial voltages and temperatures on the self-discharge rate and the variable leakage resistance value are examined, which provide some insights into the significance of model parameter variations.

2. The variable leakage resistance (VLR) model

The variable leakage resistance (VLR) model [34] is shown in Fig. 1. The first branch which includes R_1 and C_1 is the main branch. The differential capacitance C_1 is the sum of a constant capacitance C_0 and a voltage dependent capacitance $K_V * V$. The main branch, also called the immediate branch, dominates the immediate behavior of a supercapacitor in response to a charging process and captures the linear dependence of the capacitance on the terminal voltage in the practical voltage range of the device [30,31]. This branch determines the short-term voltage evolution during charge and discharge cycles. The second branch including R_2 and C_2 is the delayed branch, which represents the medium and long term charge redistribution [30,31]. The voltage relaxation is the result of charge redistribution [35]. The variable leakage resistance

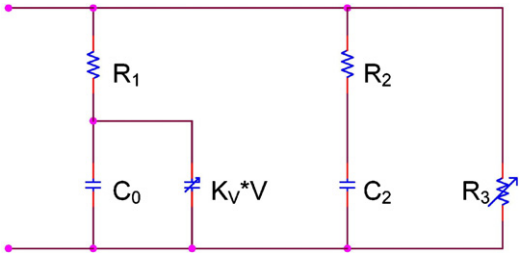

Fig. 1. The variable leakage resistance (VLR) model [34].

R_3 determines the self-discharge rate and has a value that varies with the self-discharge time [34].

The parameters of the main branch and the delayed branch can be identified by performing a two-step experiment: charging and redistribution [31]. The VLR model has been verified for supercapacitors from different manufacturers. These supercapacitors have different rated capacitances and voltages. In this paper, a 10 F supercapacitor from Panasonic with the rated voltage of 2.3 V is used as an example. As shown in Fig. 2, the 10 F supercapacitor is charged with a constant current of 100 mA to 2.3 V in 280 s during the charging phase. Once the supercapacitor is charged to its rated voltage, the charging current is turned off and the supercapacitor experiences internal charge redistribution for the following 600 s.

Assuming all the charging current is injected to the main branch in the charging phase, the resistance R_1 can be determined by the ratio of the initial voltage change ΔV to the charging current I_C:

$$R_1 = \frac{\Delta V}{I_C} \tag{1}$$

As the R_1 value identified using this approach is very close to the internal resistance value provided in the supercapacitor datasheet [36], it is reasonable to use this datasheet value for R_1. Based on the analysis of the time–voltage relationship during the charging phase, the main branch capacitances can be determined using the following equations given two data points $P_1(t_1,V_1)$ and $P_2(t_2,V_2)$ in the charging curve [31]:

$$\begin{cases} C_0 = \left[\dfrac{t_1}{V_1} - \dfrac{V_1 t_2 - t_1 V_2}{V_2^2 - V_1 V_2}\right] I_C \\ K_V = 2\left[\dfrac{V_1 t_2 - t_1 V_2}{V_1 V_2^2 - V_1^2 V_2}\right] I_C \end{cases} \tag{2}$$

During the redistribution phase, part of the charge stored in the first branch will be redistributed to the second branch [31]. If the time constant of the second branch $\tau_2 = R_2 C_2$ is fixed, we can assume the voltages of both branches are same at time $3\tau_2$. Once the time

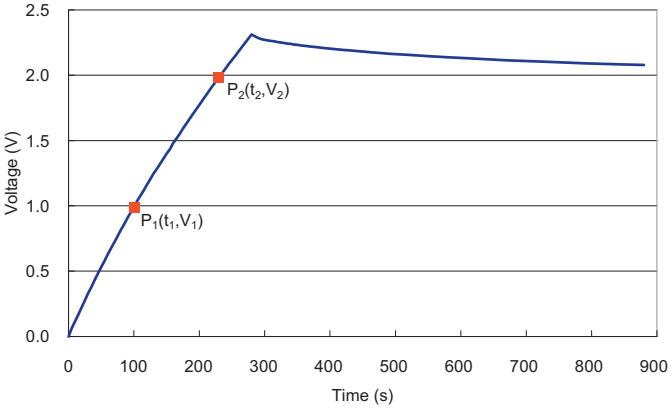

Fig. 2. Charging-redistribution of a 10 F supercapacitor.

Table 1
Model parameters of a 10 F supercapacitor.

R_1 (Ω)	C_0 (F)	K_V (F·V^{-1})	R_2 (Ω)	C_2 (F)
0.10	8.70	1.05	110	2.50

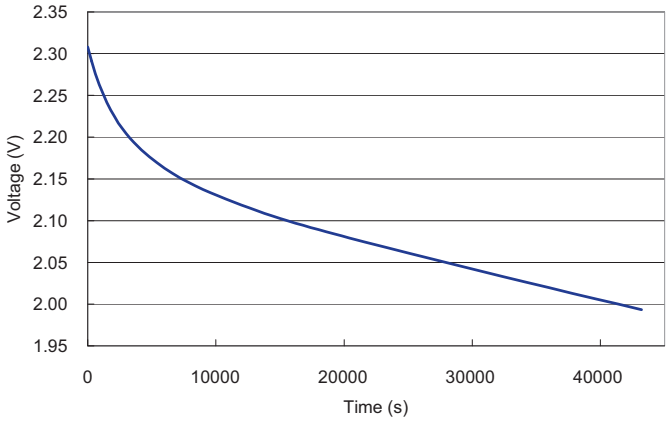

Fig. 3. Self-discharge of a 10 F supercapacitor.

constant of the second branch is determined, the voltage of the supercapacitor at time $3\tau_2$, V_{2f}, during the redistribution process can be measured. At this point, assuming all the charge is stored in the supercapacitor, C_2 can be determined from the following equation [31]:

$$Q_{\text{tot}} = I_C T_C = C_2 V_{2f} + \left(C_0 + \frac{K_V}{2} V_{2f}\right) V_{2f} \tag{3}$$

where T_C is the duration of the charging phase. The value of resistance R_2 is then calculated as follows:

$$R_2 = \frac{\tau_2}{C_2} \tag{4}$$

The values of model parameters in the first and second branches of the 10 F supercapacitor VLR model are listed in Table 1.

3. Self-discharge analysis and characterization

A charged supercapacitor is in a state of higher Gibbs energy than in its discharged state [37]. Therefore a thermodynamic "driving force" results in spontaneous decline of Gibbs energy [37]. This decline manifested as decay in supercapacitor voltage is the self-discharge. The rate of self-discharge, which is usually diminishing with time, actually determines the shelf-life of supercapacitors [38]. Fig. 3 shows the self-discharge of the 10 F supercapacitor. The open circuit voltage of the supercapacitor is measured for 12 h after it is fully charged to its rated voltage 2.3 V with a constant voltage source.

3.1. Self-discharge mechanisms

Open-circuit self-discharge of supercapacitors must take place through coupled anodic and cathodic processes to pass parasitic currents at one or both individual electrodes since there is no external circuit through which discharge can pass [37]. The self-discharge can be ascribed to three mechanisms [37–39]:

(1) A Faradaic charge-transfer reaction can occur if the voltage across an electrolyte–carbon interface exceeds the decomposition potential limit of the electrolyte. This process will result in a self-discharge process having a voltage-dependent Faradaic resistance.

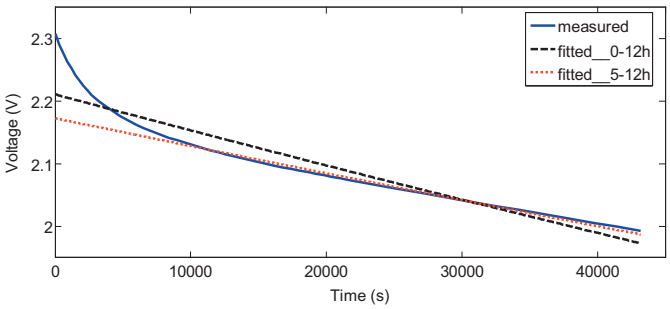

Fig. 4. Fitting self-discharge using exponential functions.

(2) A diffusion-controlled Faradaic process involving depolarization by impurity reactions, which appears to dominate the self-discharge in the first few hours. Accumulation of an excess ionic concentration can occur near the carbon–electrolyte interface if the supercapacitor is charged to a threshold voltage. When the supercapacitor is disconnected from the charging power source, part of the charge will undergo self-discharge because of the presence of impurities. The self-discharge redox process is diffusion-controlled if low concentrations of impurities are present. The Faradaic redox reactions build up a concentration of an ionic species in the electrolyte near the carbon surfaces. A simplified relationship of the supercapacitor self-discharge voltage and the initial voltage is represented by the following equation:

$$V = V_0 - m\sqrt{t} \tag{5}$$

where V is the supercapacitor voltage during the self-discharge, V_0 is the initial voltage, m is the diffusion parameter, and t is the self-discharge time.

(3) A leakage current can arise through the double-layer at the electrolyte–carbon interface if the supercapacitor has internal ohmic leakage pathways. The characteristic self-discharge behavior of this mechanism is modeled as follows:

$$V = V_0 \exp\left(-\frac{t}{R_L C}\right) \tag{6}$$

where R_L is a constant leakage resistance and C is the capacitance of the supercapacitor.

Under the normal operation conditions, the first self-discharge mechanism does not need to be modeled. The second self-discharge mechanism, the diffusion-controlled process, dominates the self-discharge in the first few hours, where the self-discharge cannot be modeled using an exponential function. Then the internal ohmic leakage becomes the dominant factor, which causes the supercapacitor voltage to decay exponentially [39]. As shown in Fig. 4, a single exponential function (the dashed curve) does not match the overall experimental data during the 12-h self-discharge. However, after 18,000 s (5 h), the supercapacitor voltage can be fitted well using an exponential function with a fixed time constant (the dotted curve). When this function is extended to the first 5 h of the self-discharge, the predicted values deviate significantly from the experimental data. Therefore, it is reasonable to adopt the variable leakage resistance in the first few hours of the self-discharge. Afterwards, the leakage resistance can be treated as a constant.

3.2. Self-discharge analysis

The fully charged supercapacitor experiences self-discharge through the variable leakage resistance after the constant voltage

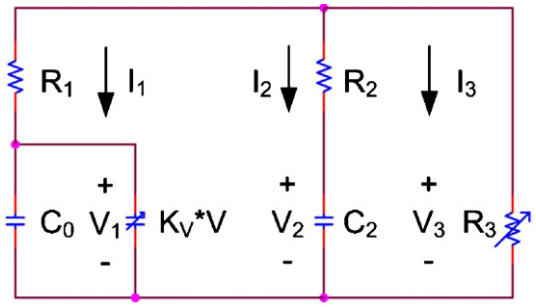

Fig. 5. Circuit for self-discharge analysis.

source is removed. The circuit used to analyze the supercapacitor terminal behavior during the self-discharge is shown in Fig. 5.

The relationship of the three branch currents can be described using the Kirchhoff's current law:

$$I_3 = -I_1 - I_2 \tag{7}$$

If we can determine the current I_3, together with the measured supercapacitor voltage profile V_3 during the self-discharge, the resistance R_3 can be calculated by the Ohm's Law:

$$R_3 = \frac{V_3}{I_3} \tag{8}$$

The main branch current I_1 is also the current through the capacitance C_1:

$$I_1 = \frac{d(C_1V_1)}{dt} = \frac{d((C_0 + K_VV_1)V_1)}{dt} = (C_0 + 2K_VV_1)\frac{dV_1}{dt} \tag{9}$$

The voltage V_1 across the capacitance C_1 is related to V_3 by the following equation:

$$V_1 = V_3 - I_1R_1 \tag{10}$$

Similarly, the current and voltage relationships for the delayed branch are:

$$I_2 = \frac{d(C_2V_2)}{dt} = C_2\frac{dV_2}{dt} \tag{11}$$

$$V_2 = V_3 - I_2R_2 \tag{12}$$

As voltages and currents of all the circuit elements are tangled, it is very difficult to derive the closed-form analytical solutions for I_3 and R_3. A numerical approach can be used to solve this system composed of Eqs. (7)–(12).

3.3. Determination of variable leakage resistance

The system composed of Eqs. (7)–(12) is implemented using MATLAB. The Simulink model is shown in Fig. 6. The input is the supercapacitor voltage profile V_3 measured during the self-discharge. The output is the variable leakage resistance R_3. The blocks representing the model parameters are annotated. For example, the constant capacitance C_0 is represented by the block "Step 1".

The leakage resistance value varies with the self-discharge time as shown in Fig. 7. As expected, during the 12-h self-discharge, the resistance value increases from 2500 Ω to 32,093 Ω in the first 5 h (0–18,000 s), and finally to 35,877 Ω at the end of this self-discharge (at 43,200 s). The increase in the resistance value during the first 5 h is the result of combined self-discharge mechanisms, including the diffusion-controlled Faradaic process and the internal ohmic leakage. The diffusion-controlled Faradaic process dominates. Consistent with the self-discharge shown in Fig. 4, after 5 h, the internal ohmic leakage takes over and a constant leakage

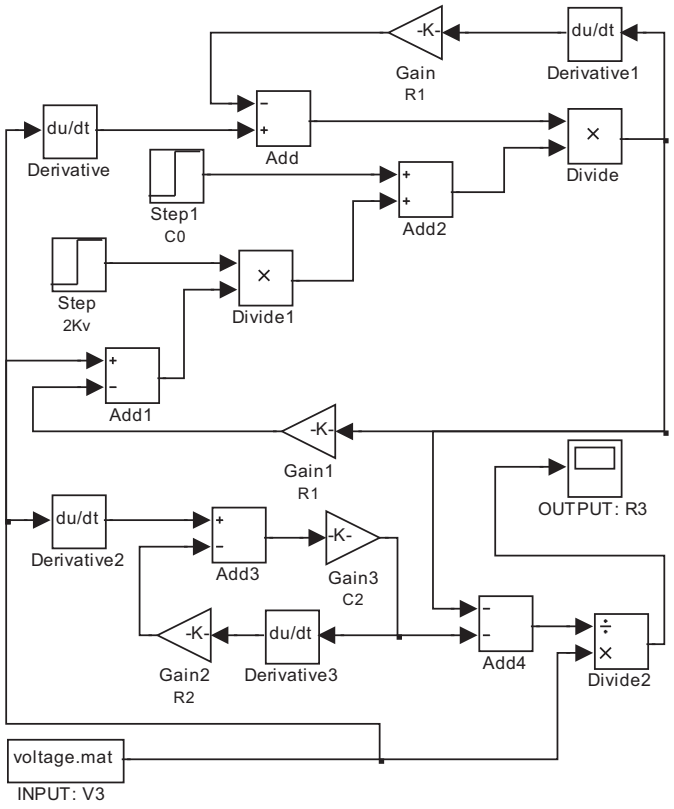

Fig. 6. Simulink implementation of variable leakage resistance determination process.

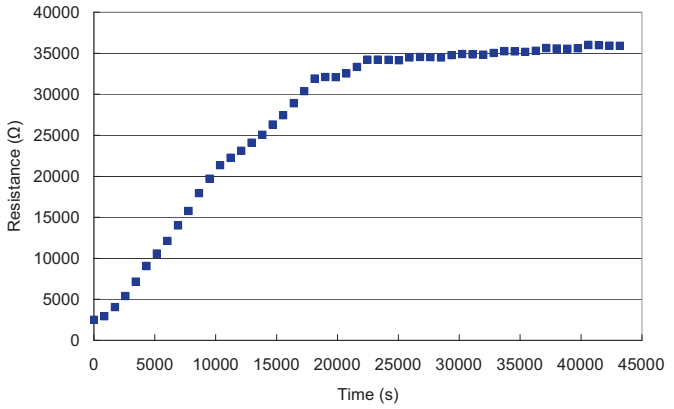

Fig. 7. Variable leakage resistance versus self-discharge time.

resistance accounts for the exponential decay of the supercapacitor voltage.

The input (terminal voltage profile) and output (variable leakage resistance) relationship demonstrated by the Simulink model shows the dependence of leakage resistance values on supercapacitor terminal voltages, as shown in Fig. 8. The resistance value increases rapidly from 2500 Ω to 32,093 Ω when the supercapacitor voltage decreases from 2.3080 V to 2.0892 V. This period corresponds to the self-discharge time of the first 5 h (0–18,000 s). The resistance value increases very slowly from 32,093 Ω to 35,877 Ω when the supercapacitor voltage decreases from 2.0892 V to 1.9934 V at the end of the 12-h self-discharge.

Although the variable leakage resistance can be related either to the self-discharge time or to the supercapacitor voltage, the latter relationship is preferred since the terminal voltage can be easily

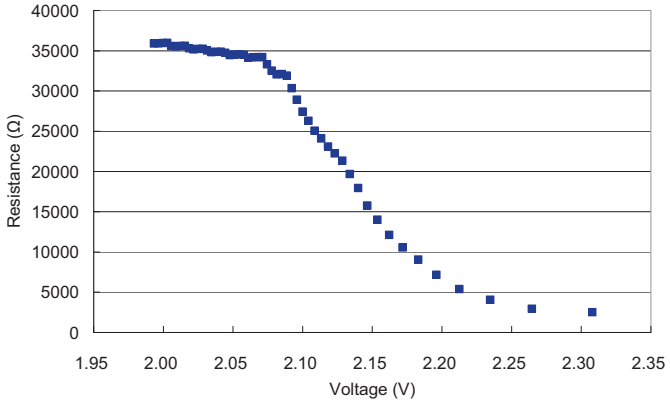

Fig. 8. Variable leakage resistance versus supercapacitor voltage.

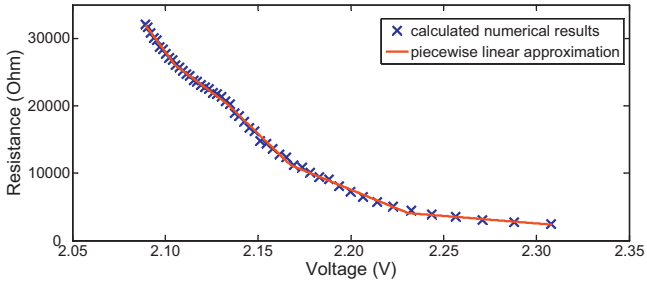

Fig. 9. Comparison between calculated and fitted variable leakage resistance.

measured. To mathematically describe the relationship between the variable leakage resistance and the supercapacitor voltage, piecewise linear approximation can be adopted. The start and end points of line segments are determined by the turning points where the resistance-voltage curve has considerable slope change. Since the resistance value only shows a very slow increase after the supercapacitor voltage is below 2.0892 V, a constant value instead of a linear function is used for this voltage range. The constant resistance value of 35,500 Ω is calculated as the average of the values for the voltage range of 1.9934–2.0892 V. The piecewise linear approximation is then only applied to the voltage range of 2.0892–2.3080 V (Eq. (13)). The piecewise linear model matches the empirical data well as shown in Fig. 9.

$$R_3 = \begin{cases} (-3.716V_3 + 8.084) \times 10^5, & V_3 = (2.0892, 2.1053) \\ (-2.044V_3 + 4.564) \times 10^5, & V_3 = (2.1053, 2.1333) \\ (-2.659V_3 + 5.876) \times 10^5, & V_3 = (2.1333, 2.1676) \\ (-1.126V_3 + 2.553) \times 10^5, & V_3 = (2.1676, 2.2310) \\ (-2.216V_3 + 5.353) \times 10^4, & V_3 = (2.2310, 2.3080 \end{cases} \quad (13)$$

4. Model validation

4.1. Model validation for self-discharge

The circuit model shown in Fig. 5 is used to predict the supercapacitor voltage profile during the self-discharge. The model parameters of the 10 F supercapacitor are listed in Table 1 and Eq. (13). For the self-discharge process, all capacitances in the model are fully charged to the supercapacitor rated voltage initially. A value of 2.3080 V is used as the initial voltage for the Simulink model which is the measured initial voltage of the self-discharge experiment. The supercapacitor voltage profile predicted by the VLR model is shown in Fig. 10 for 12 h, which matches the experimental data very well.

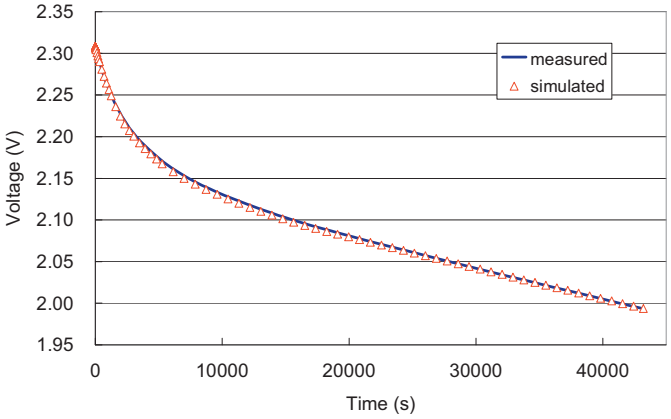

Fig. 10. Comparison between measured and simulated self-discharge.

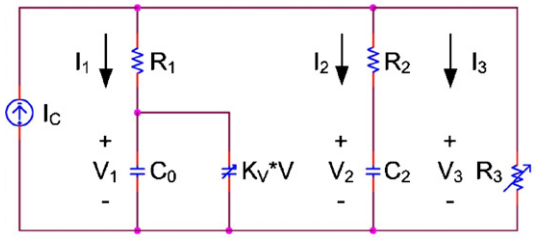

Fig. 11. Circuit for charging-redistribution analysis.

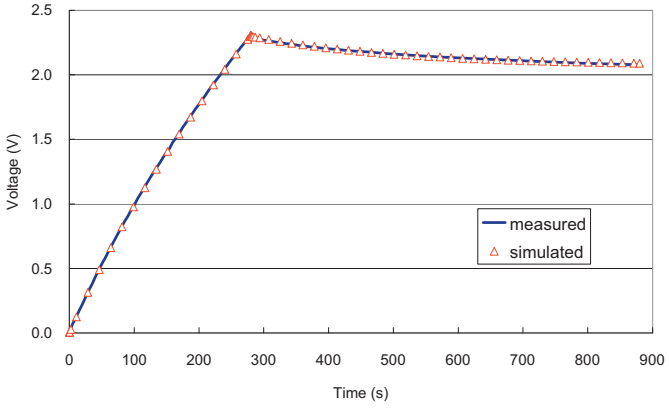

Fig. 12. Comparison between measured and simulated charging-redistribution.

4.2. Model validation for charging-redistribution

The VLR model is also validated for the charging-redistribution process. The circuit shown in Fig. 11 is used to develop the circuit element voltage and current relationships. The supercapacitor is initially discharged and all the capacitances have zero voltages. In the charging phase, the current source I_C provides a constant current of 100 mA for 280 s. Then the current source is removed and the supercapacitor experiences internal charge redistribution.

The charging current and the three branch currents are related by the following equation:

$$I_C = I_1 + I_2 + I_3 \quad (14)$$

Combining Eqs. (8)–(12) and (14), a slightly different MATLAB Simulink model can be implemented with the charging current (I_C) profile as the input. The output, the supercapacitor terminal voltage profile V_3, is predicted using the VLR model and compared with the measured data in Fig. 12. Again, the simulation results follow the measurements closely, which demonstrates that the piecewise

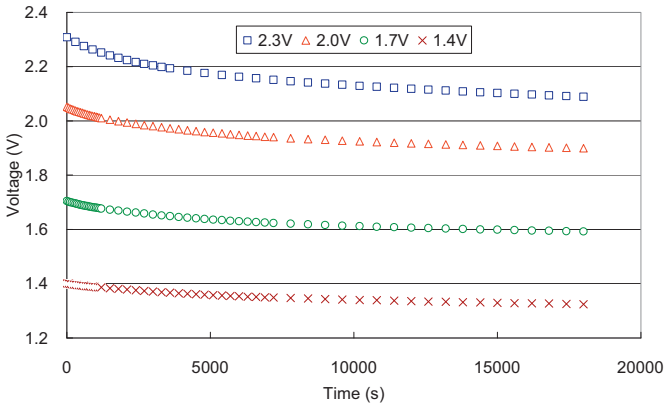

Fig. 13. Self-discharge measurements for different initial voltages.

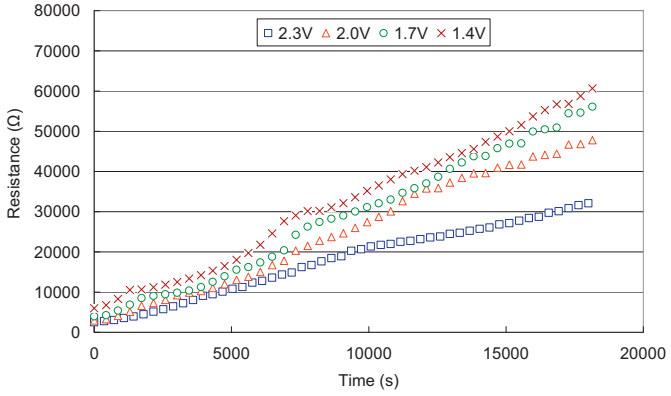

Fig. 14. Variable leakage resistance versus self-discharge time for different initial voltages.

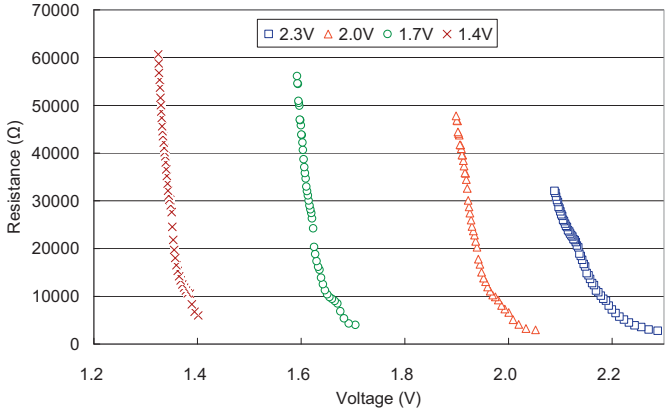

Fig. 15. Variable leakage resistance versus supercapacitor voltage for different initial voltages.

linear approximation accurately represents the resistance–voltage relationship.

5. Initial voltage dependence of self-discharge rate

To investigate the dependence of the self-discharge rate on the initial voltage across the supercapacitor, the self-discharge of the 10 F supercapacitor is measured for initial voltages of 2.3, 2.0, 1.7, and 1.4 V, respectively (Fig. 13). The self-discharge measurements are recorded only for the first 5 h because the resistance value varies greatly with the supercapacitor voltage during this period of time. After a 5-h self-discharge, the supercapacitor voltage drops by 0.2188, 0.1528, 0.1121, and 0.0767 V for initial voltages of 2.3, 2.0, 1.7, and 1.4 V, respectively. A higher initial voltage results in a faster self-discharge rate.

This dependence can be explained by the effect of the initial voltage on the diffusion parameter [39]. The diffusion parameter increases strongly with the increasing initial voltage above a threshold of about 1 V. The dependence of the diffusion parameter on the initial voltage is originated from a strong dependence of the initial excess concentration of ionic species on the initial voltage. The 10 F supercapacitor is constructed using carbon electrodes and organic electrolytes [40] which are the typical materials for most of the current supercapacitors [41]. For supercapacitors built with these materials, excess ionic concentration accumulates near the carbon surface when the initial voltage is above the threshold and develops a concentration gradient in the electrolyte [39]. As a larger initial voltage leads to higher excess ionic concentration, the diffusion parameter is also increased. As a result, a faster voltage drop rate is expected based on Eq. (5).

The variable leakage resistance values are calculated for different initial voltages. To examine the effect of the initial voltage on the leakage resistance value, both the resistance–time and resistance–voltage relationships for the four initial voltages are plotted in Figs. 14 and 15, respectively. Two major observations can be made. First, for any specific self-discharge with an initial voltage above 1 V but lower than the rated voltage of 2.3 V, the resistance–time and resistance–voltage relationships are similar to those of the self-discharge with the rated voltage as the initial voltage. Specifically, the leakage resistance value increases as the self-discharge time increases, or equivalently, the leakage resistance value increases as the supercapacitor voltage decreases. The self-discharge rate decreases as the self-discharge time elapses which leads to an increase of the resistance value. Second, it is clearly shown in Fig. 14 that the leakage resistance value increases when the initial voltage decreases for a specific self-discharge time. For example, the resistance values are 32,093, 47,792, 56,141, and 60,673 Ω at the end of the 5-h experiments for self-discharges with initial voltages of 2.3, 2.0, 1.7, and 1.4 V, respectively. This phenomenon can be also observed in Fig. 15. For a fixed self-discharge time, different initial voltages lead to different voltage drops: the lower the initial voltage, the smaller the voltage drop, and the higher the leakage resistance value.

As the leakage resistance increases with the decrease of the initial voltage, the VLR model developed from a fully charged supercapacitor will overestimate the self-discharge rate for lower initial voltages. For example, the measured and the simulated self-discharge with an initial voltage of 2.0 V are shown in Fig. 16.

The mean absolute percentage error (MAPE) defined as follows is used to quantify the average deviation of the VLR model, which

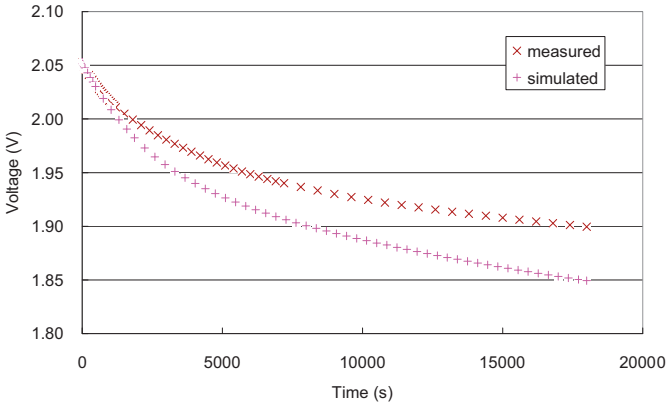

Fig. 16. Comparison between measured and simulated self-discharge for 2.0 V.

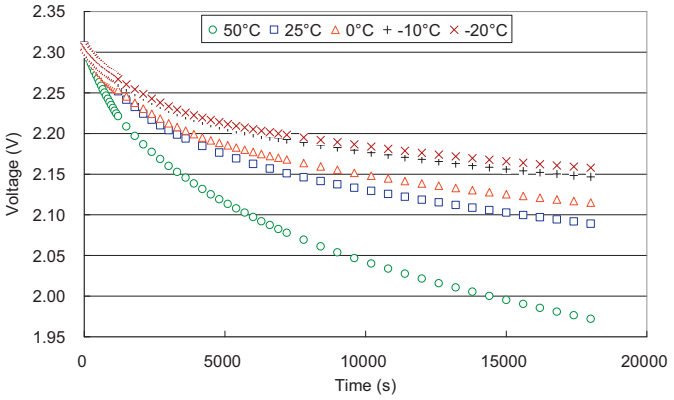

Fig. 17. Self-discharge measurements at different temperatures.

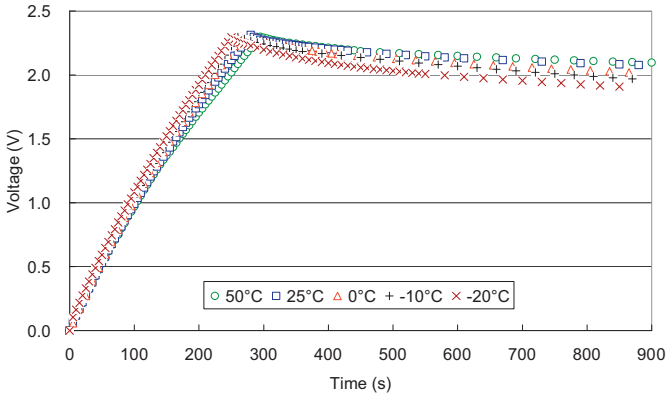

Fig. 18. Charging-redistribution measurements at different temperatures.

is developed from a fully charged supercapacitor, in the first 5-h self-discharge period for different initial voltages:

$$MAPE = \frac{1}{N}\sum_{i=1}^{N}\left|\frac{V_S(i) - V_M(i)}{V_M(i)}\right| \times 100\% \quad (15)$$

where $V_S(i)$ and $V_M(i)$ are the simulated and measured supercapacitor voltages during the self-discharge, N is the number of samples. For self-discharges with initial voltages of 2.0, 1.7, and 1.4 V, the MAPE is 1.77%, 2.84%, and 4.11%, respectively. The MAPE increases when the initial voltage decreases as a result of the increased resistance variation. Depending on specific applications, it is up to designers to determine if this resistance variation is critical. Since the VLR model developed from the fully charged supercapacitor slightly overestimates the self-discharge rate for lower initial voltages, it provides a safety margin that prevents failure of a wireless sensor node.

6. Temperature dependence of self-discharge rate

The supercapacitor self-discharge rate is also temperature dependent [39]. To examine the temperature dependence of the self-discharge rate, five self-discharge experiments are conducted at temperatures of 50, 25, 0, −10, and −20 °C for the same initial voltage of 2.3 V. As shown in Fig. 17, the self-discharge rate is faster for higher temperature. Over the 5-h self-discharge, the voltage drops for temperatures of 50, 25, 0, −10, and −20 °C are 0.3352, 0.2188, 0.1925, 0.1595, and 0.1489 V, respectively.

The self-discharge rate is dependent on the ionic transport rate [39]. An increase in the temperature accelerates this transport process, which causes excess ionic concentrations near the electrodes of the supercapacitor. As a result, the diffusion parameter increases as the temperature increases which leads to a higher self-discharge rate.

In addition to the self-discharge rate, other supercapacitor model parameters also vary with temperature. For example, the supercapacitor global capacitance depends on the electrolyte dielectric constant and the thickness of the double-layer that vary with temperature [41]. To determine the variable leakage resistance values at different temperatures, we need to first perform charging-redistribution experiments to identify the parameters of the main branch and the delayed branch. The measurements are shown in Fig. 18. The identified parameters at different temperatures are listed in Table 2.

The variable leakage resistance values are calculated for different temperatures. As shown in Figs. 19 and 20, the variable leakage resistance varies with the self-discharge time or the supercapacitor voltage in similar manners for different temperatures. When

Table 2
Model parameters at different temperatures.

	Temperature (°C)				
	50	25	0	−10	−20
R_1 (Ω)	0.10	0.10	0.11	0.12	0.14
C_0 (F)	9.50	8.70	8.20	7.60	6.95
K_V (F·V^{-1})	1.00	1.05	1.07	1.10	1.12
R_2 (Ω)	100	110	120	85	75
C_2 (F)	2.40	2.50	2.65	3.40	3.75

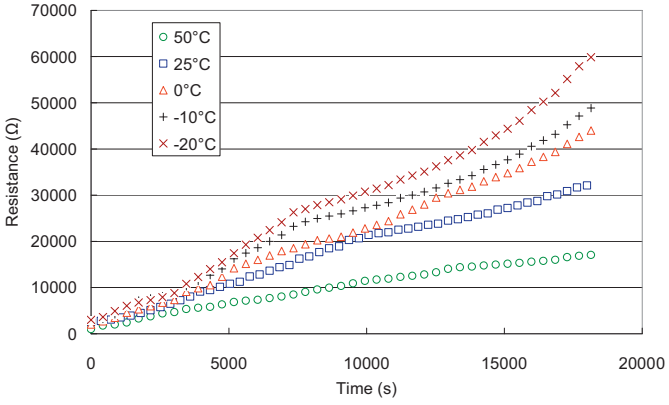

Fig. 19. Variable leakage resistance versus self-discharge time for different temperatures.

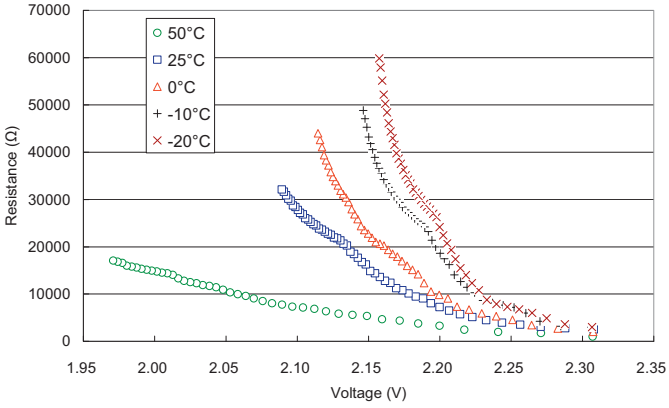

Fig. 20. Variable leakage resistance versus supercapacitor voltage for different temperatures.

the temperature decreases, the leakage resistance value increases for a specific self-discharge time (Fig. 19) or a fixed supercapacitor voltage (Fig. 20).

Using the VLR model developed at 25 °C to predict the self-discharge of the supercapacitor at 50, 0, −10, and −20 °C, the MAPE for the first 5 h is 3.65%, 0.86%, 1.97%, and 2.26%, respectively. As temperature also affects the parameters of the main branch and the delayed branch, the MAPE for the charging-redistribution is also calculated. For the charging-redistribution at temperatures of 50, 0, −10, and −20 °C, the MAPE is 3.52%, 2.81%, 4.13%, and 5.35%, respectively. If the variations fall within the error tolerances of the targeted applications, the model parameters identified through experiments at room temperature can be used for a relatively wide temperature range.

7. Conclusions

Based on the variable leakage resistance model we developed for supercapacitors targeting environmentally powered wireless sensor network applications, the supercapacitor self-discharge voltage profile is analyzed. As the variable leakage resistance is very difficult to solve analytically, a numerical approach is adopted and implemented using MATLAB Simulink. The calculated numerical results of the leakage resistance values are related to either the self-discharge time or the supercapacitor terminal voltages. A piecewise linear approximation model is used to calculate the variable leakage resistance values from the supercapacitor terminal voltages, which makes the VLR model more practical.

The dependences of the self-discharge rate and the variable leakage resistance on initial voltages and temperatures are also investigated. For all initial voltage values, the leakage resistance increases with the increase of the self-leakage time or the decrease of the supercapacitor terminal voltage. For a specific self-discharge time or terminal voltage, a higher initial voltage results in a higher self-discharge rate, therefore a lower leakage resistance value. For different temperatures, a higher temperature leads to a higher diffusion parameter. As a result, with increasing temperature, the self-discharge rate increases and the variable leakage resistance value decreases.

References

[1] T. He, S. Krishnamurthy, J. Stankovic, T. Abdelzaher, L. Luo, R. Stoleru, T. Yan, L. Gu, J. Hui, B. Krogh, Proceedings of the 2nd International Conference on Mobile Systems, Applications, and Services (MobiSys'04), June 6–9, 2004, pp. 270–283.
[2] R. Szewczyk, A. Mainwaring, J. Polastre, J. Anderson, D. Culler, Proceedings of the 2nd International Conference on Embedded Networked Sensor Systems (SenSys'04), November 3–5, 2004, pp. 214–226.
[3] B.T. Kuhn, R.S. Balog, Proceedings of the 23rd Annual IEEE Applied Power Electronics Conference and Exposition (APEC 2008), February 24–28, 2008, pp. 154–159.
[4] S. Meninger, J.O. Mur-Miranda, R. Amirtharajah, A.P. Chandrakasan, J.H. Lang, IEEE Trans. Very Large Scale Integr. (VLSI) Syst. 9 (2001) 64–76.
[5] T. Le, K. Mayaram, T. Fiez, IEEE J. Solid-State Circ. 43 (2008) 1287–1302.
[6] Y.K. Tan, S.K. Panda, Proceedings of the 33rd Annual Conference of the IEEE Industrial Electronics Society (IECON 2007), November 5–8, 2007, pp. 2175–2180.
[7] J. Taneja, J. Jeong, D. Culler, Proceedings of the 7th International Conference on Information Processing in Sensor Networks (IPSN'08), April 22–24, 2008, pp. 407–418.
[8] P. Zhang, C.M. Sadler, S.A. Lyon, M. Martonosi, Proceedings of the 2nd International Conference on Embedded Networked Sensor Systems (SenSys'04), November 3–5, 2004, pp. 227–238.
[9] F. Simjee, P.H. Chou, Proceedings of the 2006 International Symposium on Low Power Electronics and Design (ISLPED'06), October 4–6, 2006, pp. 197–202.
[10] T. Umemura, Y. Mizutani, T. Okamoto, T. Taguchi, K. Nakajima, K. Tanaka, Proceedings of the 7th International Conference on Properties and Applications of Dielectric Materials, June 1–5, 2003, pp. 944–948.
[11] GP Batteries Nickel Metal Hydride Technical Handbook. http://www.gpbatteries.com/html/pdf/NiMH_technical.pdf.
[12] T. Zhu, Z. Zhong, Y. Gu, T. He, Z. Zhang, Proceedings of the 7th International Conference on Mobile Systems, Applications and Services (MobiSys'09), June 22–25, 2009, pp. 319–332.
[13] D. Brunelli, C. Moser, L. Thiele, L. Benini, IEEE Trans. Circ. Syst. I Reg. Papers 56 (2009) 2519–2528.
[14] X. Jiang, J. Polsatre, D. Culler, Proceedings of the 4th International Symposium on Information Processing in Sensor Networks (IPSN'05), April 15, 2005, pp. 463–468.
[15] J. Alberola, J. Pelegri, R. Lajara, J.J. Perez, Proceedings of the IEEE Instrumentation and Measurement Technology Conference, May 12–15, 2008, pp. 657–662.
[16] C. Moser, J. Chen, L. Thiele, Proceedings of the 14th ACM/IEEE International Symposium on Low Power Electronics and Design (ISLPED'09), August 19–21, 2009, pp. 413–418.
[17] A. Kailas, M. Ingram, Y. Zhang, Proceedings of the 1st International Conference on Wireless Communication, Vehicular Technology Information Theory and Aerospace & Electronic Systems Technology, May 17–20, 2009, pp. 42–46.
[18] S. Buller, E. Karden, D. Kok, R.W. De Doncker, IEEE Trans. Ind. Appl. 38 (2002) 1622–1626.
[19] W. Lajnef, J.-M. Vinassa, O. Briat, S. Azzopardi, E. Woirgard, J. Power Sources 168 (2007) 553–560.
[20] F. Rafik, H. Gualous, R. Gallay, A. Crausaz, A. Berthon, J. Power Sources 165 (2007) 928–934.
[21] D. Riu, N. Retiere, D. Linzen, Conference Record of the 2004 IEEE Industry Applications Conference, October 3–7, 2004, pp. 2550–2554.
[22] A.G. Pandolfo, A.F. Hollenkamp, J. Power Sources 157 (2006) 11–27.
[23] A. Celzard, F. Collas, J.F. Mareche, G. Furdin, I. Rey, J. Power Sources 108 (2002) 153–162.
[24] N. Bertrand, J. Sabatier, O. Briat, J.-M. Vinassa, IEEE Trans. Ind. Electron. 57 (2010) 3991–4000.
[25] G. Paasch, K. Micka, P. Gersdorf, Electrochim. Acta 38 (1993) 2653–2662.
[26] E.-H. El Brouji, O. Briat, J.-M. Vinassa, N. Bertrand, E. Woirgard, IEEE Trans. Veh. Technol. 58 (2009) 3917–3929.
[27] G. Sikha, R.E. White, B.N. Popov, J. Electrochem. Soc. 152 (2005) A1682–A1693.
[28] H.-K. Song, H.-Y. Hwang, K.-H. Lee, L.H. Dao, Electrochim. Acta 45 (2000) 2241–2257.
[29] F. Belhachemi, S. Rael, B. Davat, Conference Record of the 2000 IEEE Industry Applications Conference, October 8–12, 2000, pp. 3069–3076.
[30] L. Zubieta, R. Bonert, IEEE Trans. Ind. Appl. 36 (2000) 199–205.
[31] R. Faranda, Elect. Power Syst. Res. 80 (2010) 363–371.
[32] Y. Diab, P. Venet, H. Gualous, G. Rojat, IEEE Trans. Power Electron. 24 (2009) 510–517.
[33] G.V. Merrett, A.S. Weddell, A.P. Lewis, N.R. Harris, B.M. Al-Hashimi, N.M. White, Proceedings of 17th International Conference on Computer Communications and Networks, August 3–7, 2008, pp. 1–6.
[34] Y. Zhang, H. Yang, J. Power Sources 196 (2011) 4128–4235.
[35] H. El Brouji, J.-M. Vinassa, O. Briat, N. Bertrand, E. Woirgard, Proceedings of the 2008 IEEE Vehicle Power and Propulsion Conference, September 3–5, 2008, pp. 1–6.
[36] Panasonic Electric Double Layer Capacitors HW Series Datasheet. http://industrial.panasonic.com/www-cgi/jvcr13pz.cgi?E+PZ+3+ABC0008+EECHW0D106+7+WW.
[37] J. Niu, B.E. Conway, W.G. Pell, J. Power Sources 135 (2004) 332–343.
[38] B.E. Conway, Electrochemical Supercapacitors: Scientific Fundamentals and Technological Applications, Kluwer Academic/Plenum Publishers, 1999.
[39] B.W. Ricketts, C. Ton-That, J. Power Sources 89 (2000) 64–69.
[40] Panasonic Electric Double Layer Capacitors Principles and Features. http://industrial.panasonic.com/www-data/pdf/ABC0000/ABC0000TE2.pdf.
[41] A. Burke, J. Power Sources 91 (2000) 37–50.